



External cavity quantum cascade laser emitting from 12.3 to 13.2 μm

Sylvain Mathonnière¹ · Ján Tomko¹ · Yohei Matsuoka¹ · Sven Peters² · Jan Kischkat¹ · Mykhaylo Semtsiv¹ · W. Ted Masselink¹

Received: 31 January 2018 / Accepted: 23 June 2018 / Published online: 28 June 2018
© Springer-Verlag GmbH Germany, part of Springer Nature 2018

Abstract

We describe a long-wavelength external cavity quantum cascade laser, emitting from 12.3 to 13.2 μm integrated into a compact design to promote portability. For this purpose, a new type of anti-reflection coating was designed as well as a new way of measuring its performance. Finally, a portion of the absorption spectrum of ammonia vapor was recorded by tuning the laser, which demonstrates the spectroscopic capacity of this EC-QCL.

1 Introduction

The quantum cascade laser (QCL) first demonstrated in 1994 [1] has proved itself to be a very versatile source of infrared radiation from below 3 μm [2, 3] up to 24 μm [4] in the mid infrared region and from 0.84 to 5 THz [5, 6] in the THz region. For spectroscopy applications, gas sensing, countermeasures, and hyperspectral imaging, a variety of tunable QCLs have been realized, mainly in the range from 4 to 12 μm , in the configuration of external cavity quantum cascade laser (ECQCL) [7–9]. Some chemical compounds, however, have spectroscopically important absorption peaks in the spectral region beyond 12 μm . This is the case for substances such as polychlorinated biphenyl congeners (PCB), which were widely used in the past as a fire retardant but proved to be carcinogenic. The main challenge for integrating a long-wavelength QCL into an external cavity is the deposition of an efficient anti-reflection (AR) coating. Residual reflectance limits the power of the single external cavity mode as well as the tuning range. It is also not straightforward to measure the residual reflectance of the AR coating because, for well-designed AR coatings, the AR-coated laser

stripe behaves more like a superluminescent diode. In this article, we demonstrate and characterize a new AR coating for the 10–14 μm part of the spectrum, as well as its application for a long-wavelength tunable external cavity QCL.

The QCL structure used in this study was grown using gas-source molecular beam epitaxy (GSMBE) lattice matched to a low-doped ($1.10^{17} \text{ cm}^{-3}$) InP substrate following the active region design as in [10] and with the capping layers and fabrication as described in [11]. The stripe width of 15 μm was defined by wet etching. We sputtered 1 μm of SiO_2 on top of the ridge as an insulation layer and opened up a 10 μm window through the SiO_2 with dry etching. The top electrical contacts are thermally evaporated Cr/Au (20/200 nm) followed by galvanic Au. The back contacts are galvanically deposited Sn. The chip was cleaved into 6-mm-long stripes.

2 Anti-reflection coating

To prevent competing Fabry–Perot modes, it is necessary to apply an AR coating onto the intracavity facet. Commercially available AR coatings, for example on lenses or mirrors, although excellent, are mainly designed for wavelengths much shorter than 12 μm . For our application, we need a custom AR coating that will allow us to tune over the broadest part of our gain region. Using the standard transfer matrix method (TMM), we designed an AR coating based on two materials, YbF_3 and ZnS , which both exhibit low losses at those long wavelengths (Table 1). Our coating is a simple two-layer coating, the so-called V-type coating (the V representing the spectral response of the coating). We chose

This article is part of the topical collection “Mid-infrared and THz Laser Sources and Applications” guest edited by Wei Ren, Paolo De Natale and Gerard Wysocki.

✉ Sylvain Mathonnière
sylvain.mathonniere@physik.hu-berlin.de

¹ Humboldt University of Berlin, Newtonstrasse, 15, 12489 Berlin, Germany

² Sentench GmbH, Schwarzschildstraße 2, 12489 Berlin, Germany

Table 1 Anti-reflection coating composition and measured value of n and k for the material used

Layer	AR coating			
	Material.	Thk. (nm)	n (at 13 μm)	k (at 13 μm)
Substrate	InP		3.0	6.10^{-4}
Adhesion layer	Y_2O_3	10	2.43	0.35
1st layer of AR	YbF_3	878	1.27	8.10^{-3}
Adhesion layer	Y_2O_3	10	2.43	0.35
2nd layer of AR	ZnS	602	2.17	2.10^{-3}

Dispersion around 13 μm is low for n - k value of all materials, but was nevertheless included for simulations

this coating since it shows optimal performance around one specific wavelength and does not require to deposit too thick layers which could lead to mechanical deterioration of the coating [12].

The Y_2O_3 layers act as adhesion promoters for the subsequent layer to prevent any flaking or delaminating of the coating. We deposited the AR coating using electron beam deposition on a semi-insulating double-sided polished InP substrate used to measure the coating performance which is describe below. Our electron beam deposition system was calibrated by measuring the thickness of layers with ellipsometry which ensure that uncertainties of the layers thickness are below 5%. Moreover, the coating used has the advantage of having performances relatively insensitive to small variations of thicknesses and of effective refractive index of the active region, which was estimated to be around 3.1 at 13 μm .

Various techniques have been used to measure the reflectance of AR coatings that are on the facets of QCLs or laser diodes. These techniques include using the threshold current shift after coating, the change in slope efficiency between coated and non-coated facets [13], and fitting the power intensity characteristic itself before and after the coating [14]. If one knows the waveguide loss, it is also possible to evaluate the coating reflectance by cleaving the chip in several lengths and measuring the threshold current density. Unfortunately, all those techniques have more or less severe built-in inaccuracies [14] because they rely on measurements of characteristics that are not properly defined for very low reflectance or with low accuracy. Moreover, those techniques only measure the reflectance at the lasing wavelength of the chip in Fabry–Perot mode and do not allow the measurement of the reflectance along the gain region which is of tremendous importance for our application. In this manuscript, we employ a different strategy based on fitting the transmission data to Eq. 1, which represents the transmission from transparent media (1)–(3) through an absorbing medium (2). This technique has been used in the past [15]; this investigation introduces ellipsometry data into

the study to be included with the FTIR transmission data for the sake of greater accuracy in the derivation of the AR coating performance since we do not need to infer the reflectivity of the uncoated substrate which is implied in [15].

The transmission is given by

$$T = \frac{T_{12}T_{23}e^{-\alpha d}}{1 + R_{12}R_{23}e^{-2\alpha d}}, \quad (1)$$

where T_{ij} and R_{ij} represent the transmissivity and reflectivity in power at the interface between medium i and j . The absorption coefficient of layer (2) is α and d its thickness. In our case, (1) and (3) represent air and (2) is the InP substrate (coated or not). We measure the transmission of two double-sided polished InP substrates, one without any coating and one with an AR coating on one side using an FTIR. We obtain the absorption coefficient α of the substrate using the extinction coefficient data measured by ellipsometry (SENDIRA system, Sentech Instrument GmbH). By combining the transmission measurements of the FTIR and the ellipsometry data, we extract the reflectance of the AR coating using Eq. 1. Since all our measurements are wavelength dependent, we obtain the reflectance of the AR coating as a function of wavelength as shown on Fig. 1b.

By looking at the transmittance data of the uncoated InP substrate, we can observe some small absorption dips around 12.4 and 12.8 μm (Fig. 1). The absorption features are small in intensity and do not appear in the ellipsometry measurement; the origin of those absorption features are not clear, they could be due to some impurity absorption in the substrate or some Fabry–Perot oscillations between optical components in the FTIR. We use the TMM simulation model to simulate our data, but to take into account those absorption features, we fit them by adding their contributions to the extinction coefficient of the substrate measured by ellipsometry. Our model is, thus, able to accurately reproduce our measured data.

It is worth noting that outside the wavelength range of those absorption features, those absorption dips do not interfere in the calculation and would allow a direct calculation without any fitting.

This measurement method, combining FTIR transmission data with absorption measured through ellipsometry, is applicable for any range of wavelength. It was used successfully in one of our previous articles [16] and can also be used with a substrate other than InP; for example, Ge.

For further integration into external cavity, we applied this AR coating to a QCL facet and measured its threshold current density before and after coating. The threshold current depends on the facet reflectance as

$$J_{\text{th}} = \frac{\alpha_m + \alpha_w}{g\Gamma} = \frac{1}{g\Gamma} \left(\alpha_w - \frac{\ln(R_1)}{2L} \right) - \frac{\ln(R_2)}{2L}, \quad (2)$$

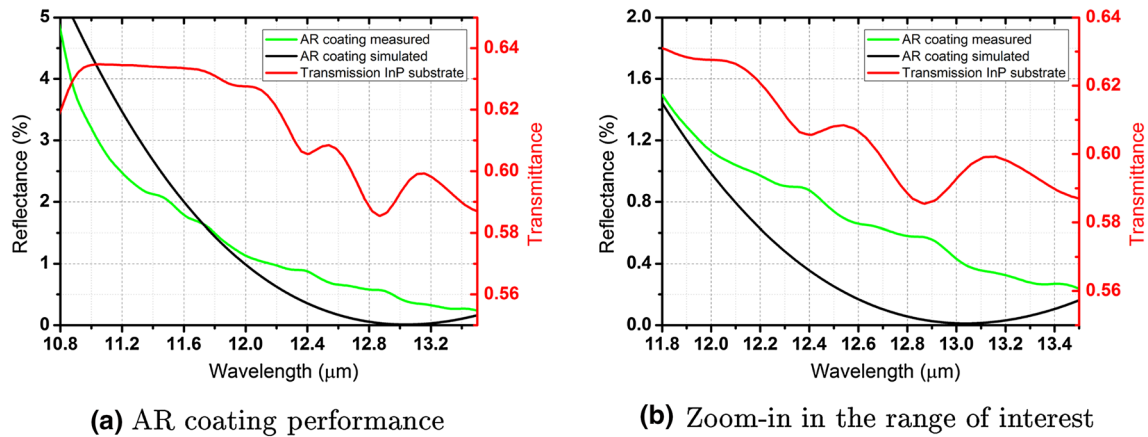


Fig. 1 The green curve corresponds to the AR coating performance obtained with YbF_3 and ZnS on a test double-sided polished InP substrate. It was calculated using the extinction coefficient data measured by ellipsometry (SENTECH Instruments GmbH) as well as transmission measurements obtained by Fourier transform infrared spectrom-

eter (FTIR). The red curve corresponds to the transmission of a bare double-side polished InP substrate ($480 \mu\text{m}$ thick) used as test for AR coating and thickness calibration. The Fabry–Perot oscillations due to the substrate thickness are not visible because the resolution of the FTIR used for the measurement is lower than their period

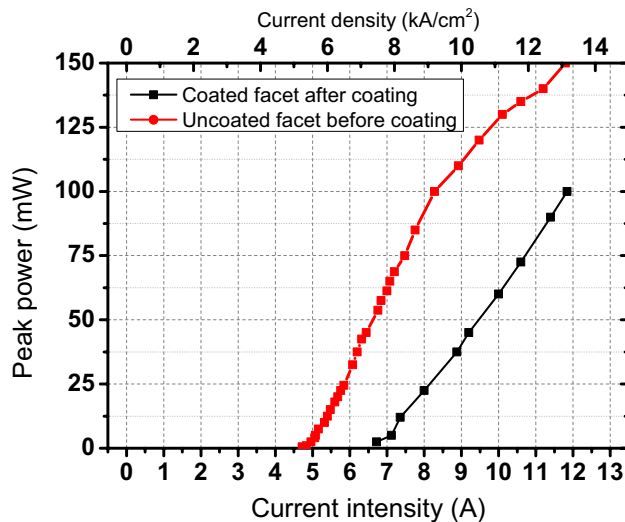


Fig. 2 Peak power intensity measurement on a 6-mm-long stripe before and after the AR coating at room temperature. The repetition rate was 0.4%

where J_{th} is the threshold current density, α_m and α_w are, respectively, the mirror loss and the waveguide loss, L is the length of the chip, g is the gain, and Γ is the confinement factor of the active region. R_1 and R_2 represent the reflectance in power of the two facets of the QCL chip. Equation 2 shows that a decrease of reflectivity translates into an increase of threshold current, since we effectively worsen our laser resonator. Figure 2 shows the typical power intensity curves before and after coating. The shift in threshold current is clearly noticeable, from ≈ 5 to $\approx 6.5 \text{ kA}/\text{cm}^2$. It is theoretically possible to extract a value of reflectance of a coated facet R_{AC} using Eq. 2 and compare the threshold

current density $J_{\text{th,AR}}$ for a laser with one facet AR-coated and the threshold current density $J_{\text{th,NC}}$ of a laser without any coating. In this case, we can transform equation 2 into: $R_{\text{AR}} = R_{\text{NC}}^{(2X-1)} e^{2L\alpha_w(1-X)}$, where R_{NC} is the reflectance of a non-coated facet and X the ratio of the threshold current density $X = \frac{J_{\text{th,AR}}}{J_{\text{th,NC}}}$. However, this expression depends heavily

on an accurate measurement of the threshold currents and of the waveguide loss since they both appear in an exponential function. Moreover, for small values of reflectance, superluminescent emission from the stripe prevents a very accurate measure of the reflectance with this method. In the end, we consider our reflectance to be given by Fig. 1b since the waveguide effective refractive index is very similar to the one of our InP substrate (3.1 and 3, respectively). Indeed, our simulations shows that a small change of refractive index of the substrate (being an InP wafer or a waveguide) will not be measurable due to the 5% error in the e-beam deposition system.

3 Integration in external cavity

After attenuating Fabry–Perot modes with the AR coating on one facet, the external cavity goal is to provide a wavelength-selective feedback in place of the AR-coated facet, allowing us to control the output wavelength of our QCL. A 100 grooves/mm reflective grating from Dynasil and a piezoelectric motor for rotating it were used for this purpose forming an external cavity 4-cm long. The external cavity was chosen to be in Littrow configuration to achieve maximum output power. The light leaving the facet facing the grating is collimated with a lens before impinging on the grating where only the filtered

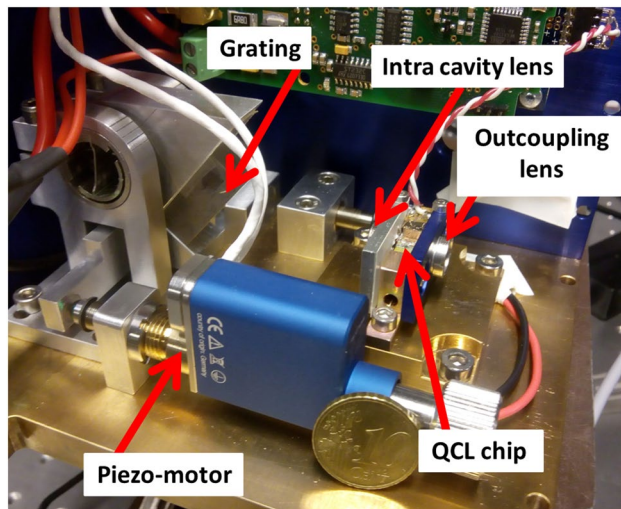


Fig. 3 Photography of our compact EC-QCL setup introducing its main components. The external cavity length is 4 cm

wavelengths will be reflected back into the QCL chip. Figure 3 shows the aforementioned components of our compact external cavity.

External cavity QCLs (EC-QCLs) are usually quite bulky because of the grating and its rotation motor. For this article, we tried to make the design as compact as possible. The full laser unit is represented in Fig. 3. The compactness is achieved by mounting the lens holder directly to the QCL mount and by using a small piezo-motor with feedback loop from PI (model N-472). The pulse generator is from Quantiox, whereas the pulse amplifier is a model from Picolas (LDP-V 50-100 V3). To improve heat extraction of our QCL, we mounted the chip epilayer down. For this purpose, we use an AlN sub-mount, which provides a room coefficient of thermal expansion similar to that of InP ($4.6 \times 10^{-6} \text{ K}^{-1}$) and good thermal conductivity of $150 \text{ W m}^{-1} \text{ K}^{-1}$ at room temperature. Our AlN sub-mounts are covered with a near eutectic mixture of Au and Sn: 76 wt% of gold and 24 wt% of tin, while the eutectic composition is 80/20 in weight, which is achieved while soldering it on our chip due to diffusion of tin and gold on the top contact made of gold. When heating both the chip and the sub-mount above the eutectic temperature of 280°C , an excellent electrical and thermal contact is achieved. The whole system is as compact as our electronic circuitry allows: ($L = 14 \text{ cm} \times H = 11 \text{ cm} \times W = 11 \text{ cm}$) and weights around 1.5 kg.

4 Characterization

4.1 Beam profile

The processing of our laser was oriented toward achieving single lobe lasing for spectroscopy utilization; to this end, a narrow stripe width of $15 \mu\text{m}$ was used. Because of this narrow width, we had to compromise on maximum power and threshold current for the sake of beam quality. Practically, it is not possible to have the facet of the stripe as wide as it is high due to the extremely long MBE growth time needed. It is therefore not possible to fully collimate both axis of the laser with one aspherical lens because of the inherent astigmatism of the QCL emission. The beam profile of our collimated laser was characterized using a chopped pyrometer camera from Ophir and was recorded at 20 cm from the emitting facet. Figure 4 shows the beam profile after collimation through an aspherical lens. A single lobed beam profile was recorded as designed. The estimated beam size at 20 cm from the facet is $1.5 \text{ mm} \times 1.0 \text{ mm}$. Because of a small astigmatism, an elliptical shape is produced as expected but with a relatively low eccentricity due to the small width of the stripe. The large diverging angle of the beam from the facet results in a high numerical aperture ($\text{NA} \approx 0.8$), resulting in a system that is extremely sensitive to lens positioning and subject to stray light visible around the beam.

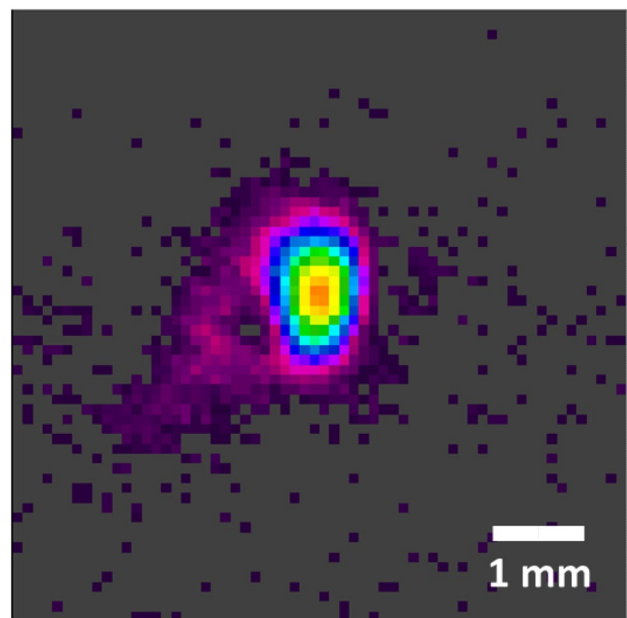


Fig. 4 Beam profile at 20 cm from the beam profiler. Beam profile of collimated light emitted from the facet recorded at 20 cm recorded with a chopped pyrometer camera from Ophir. Collimating lens characteristics: $f = 1.873 \text{ mm}$ and $\text{NA} = 0.85$. The horizontal axis is parallel to the growth direction of the QCL

4.2 Spectrum calibration

As outlined above, the tuning of the external cavity is performed by rotating a grating with a piezo-motor with encoder (N-472 from PI) whose repeatability is $0.2\ \mu\text{m}$, which translates into a grating angle of $1.6''$ giving a theoretical accuracy of $0.014\ \text{cm}^{-1}$. To calibrate the position of the motor with the actual wavelength of emission of the QCL, the motor positions are translated into rotation angles for the grating as a first step. Then, to precisely associate angles with laser emission wavenumbers, we perform a spectroscopy measurement by scanning through absorption lines of ammonia (NH_3). Using the HITRAN database of ammonia [17], and matching the absorption dips in power as seen in Fig. 5, which is equivalent to doing a linear fitting, we can precisely associate motor positions with emission wavelengths.

For this experiment, as shown in Fig. 6, the accuracy of the complete fitting is below $0.5\ \text{cm}^{-1}$. The laser was operated at $13\ \text{kA}/\text{cm}^2$ and presents mode competition between the external cavity modes (EC modes) since the spectral response FWHM of the grating was estimated at $2.6\ \text{cm}^{-1}$ which encompasses several EC modes. Though we operate our EC-QCL above the threshold current density of the FP mode of the AR-coated chip, we do not believe the FP modes inside the QCL impact much the EC operation. Faist showed [18] that at the beginning of the pulse, mode competition

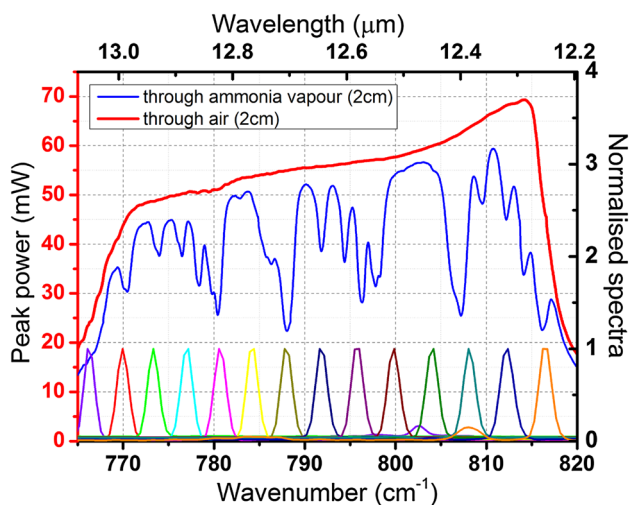


Fig. 5 Power spectra of EC-QCL measured through 2 cm of air and through ammonia vapor. The ammonia absorption peaks were used for calibration of the spectral axis. Also visible are several spectra recorded with an FTIR for different grating positions which show the single wavelength emission feature. The spectra emitting primarily below $770\ \text{cm}^{-1}$ display another feature at $802\ \text{cm}^{-1}$ which is attributed to a parasitic Fabry–Perot mode appearing since we are at the end of the tuning range. The same behavior is visible for the pulse emitting primarily above $815\ \text{cm}^{-1}$, with a parasitic Fabry–Perot mode around $808\ \text{cm}^{-1}$

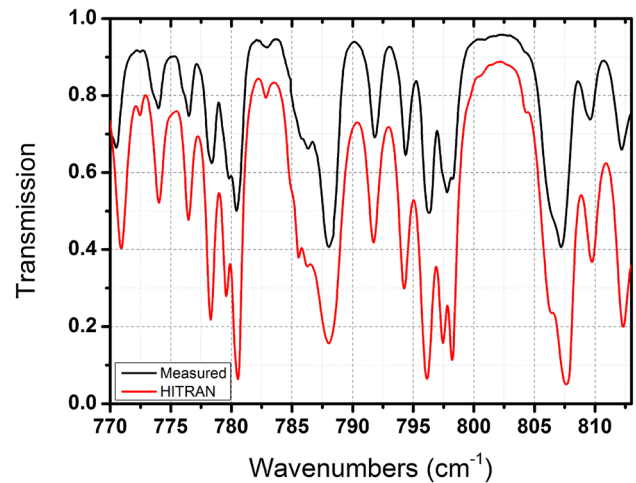


Fig. 6 Power transmission peaks at room temperature normalized and compared to the Voigt transmission profile of ammonia (NH_3) (path length 2 cm) from the HITRAN database

will appear between the FP modes and the EC modes, but that eventually (after 10 ns) the EC modes will suppress the FP modes. On the edges of the tuning range, however, we can notice (Fig. 5) the parasitic FP modes stemming from the high current density used, as mentioned in the caption of Fig. 5. It was not possible to extract properly the linewidth of the laser using the FTIR spectral measurement because of the too low resolution of our FTIR ($1\ \text{cm}^{-1}$); therefore, the linewidth was estimated at $0.7\ \text{cm}^{-1}$ by comparing the absorption curve of NH_3 measured against simulations. It is worth pointing out that this value corresponds well to typical linewidth values of the pulsed EC-QCL laser. Indeed, due to the temperature increase in the QCL chip during the pulse as well as mode competition between EC mode appearing during the pulse itself, it is very difficult to improve significantly the linewidth. The most straightforward way to improve drastically the linewidth would be by using a continuous wave laser. Finally, the purpose of this spectroscopy measurement was to calibrate properly the EC-QCL and not to accurately describe the absorption peak intensity which would be beyond the scope of this paper.

5 Conclusion

We have demonstrated and characterized a new AR coating for the $10\text{--}14\ \mu\text{m}$ part of the spectrum, as well as its application for a long-wavelength tunable external cavity QCL. The design methodology and characterization can also be applied for partially reflective coating. The EC-QCL, emitting from 12.3 to $13.2\ \mu\text{m}$ was integrated into a compact design. Such a tuning range was only possible with an adequate anti-reflection coating. For this purpose, a new type of AR coating was

designed as well as a new way of measuring its performance. The reflectance of the facet was around 1% over the entire tuning range. Finally, a portion of the absorption spectrum of ammonia vapor was recorded by tuning the laser, which demonstrates the spectroscopic capacity of this EC-QCL.

Acknowledgements The authors thank Dr. Sascha Kalusniak for the FTIR measurement. This work was supported by the Mid-TECH project which has received funding from the European Union's Horizon 2020 Research and Innovation Program under Grant Agreement No. 642661.

References

1. J. Faist, F. Capasso, D. Sivco, C. Sirtori, A.L. Hutchinson, A.Y. Cho, Quantum cascade lasers. *Science* **264**(5158), 553–556 (1994). <https://doi.org/10.1126/science.264.5158.553>
2. O. Cathabard, R. Teissier, J. Devenson, J.C. Moreno, A.N. Baranov, Quantum cascade lasers emitting near 2.6 μm . *Appl. Phys. Lett.* **96**(14), 141110 (2010)
3. M.P. Semtsiv, M. Wienold, S. Dressler, W.T. Masselink, Short-wavelength ($\lambda \approx 3.05\mu\text{m}$) inp-based strain-compensated quantum-cascade laser. *Appl. Phys. Lett.* **90**(5), 051111 (2007). <https://doi.org/10.1063/1.2437108>
4. K. Ohtani, M. Beck, J. Faist, Double metal waveguide InGaAs/InAlAs quantum cascade lasers emitting at 24 μm . *Appl. Phys. Lett.* **105**(12), 121115 (2014)
5. G. Scalari, C. Walther, M. Fischer, M. I. Amanti, R. Terazzi, N. Hoyler, H. Beere, D. Ritchie, J. Faist, Recent progress on long wavelength quantum cascade lasers between 1–2 THz. in *LEOS 2007—IEEE Lasers and Electro-Optics Society Annual Meeting Conference Proceedings*, pp. 755–756 (2007)
6. A.W.M. Lee, Q. Qin, S. Kumar, B.S. Williams, Q. Hu, J.L. Reno, Real-time terahertz imaging over a standoff distance (>25meters). *Appl. Phys. Lett.* **89**(14), 141125 (2006)
7. D. Mammez, C. Stoeffler, J. Cousin, R. Vallon, M. Mammez, L. Joly, B. Parvitte, V. Zéninari, Photoacoustic gas sensing with a commercial external cavity-quantum cascade laser at 10.5 μm . *Infrared Phys. Technol.* **61**(Supplement C), 14–19 (2013)
8. A. Kachanov, S. Koulikov, F.K. Tittel, Cavity-enhanced optical feedback-assisted photo-acoustic spectroscopy with a 10.4 μm external cavity quantum cascade laser. *Appl. Phys. B* **110**(1), 47–56 (2013)
9. A. Hugi, R. Terazzi, Y. Bonetti, A. Wittmann, M. Fischer, M. Beck, J. Faist, E. Gini, External cavity quantum cascade laser tunable from 7.6 to 11.4 μm . *Appl. Phys. Lett.* **95**(6), 061103 (2009). <https://doi.org/10.1063/1.3193539>
10. X. Huang, W.O. Charles, C. Gmachl, Temperature-insensitive long-wavelength ($\lambda \approx 14\mu\text{m}$) quantum cascade lasers with low threshold. *Opt. Express* **19**, 8297–8302 (2011). <https://doi.org/10.1364/OE.19.008297>
11. S. Mathonnière, M. Semtsiv, W.T. Masselink, Thermal annealing of lattice-matched InGaAs/InAlAs quantum-cascade lasers. *J. Cryst. Growth* **477**, 258–261 (2017). <https://doi.org/10.1016/j.jcrysgro.2017.01.029>
12. J. Kischkat, S. Peters, M.P. Semtsiv, T. Wegner, M. Elagin, G. Monastyrskyi, Y. Flores, S. Kurllov, W.T. Masselink, Ultra-narrow angle-tunable fabry perot bandpass interference filter for use as tuning element in infrared lasers. *Infrared Phys. Technol.* **67**, 432–435 (2014). <https://doi.org/10.1016/j.infrared.2014.08.020>
13. J. Nguyen, J.S. Yu, A. Evans, S. Slivken, M. Razeghi, Optical coatings by ion-beam sputtering deposition for long-wave infrared quantum cascade lasers. *Appl. Phys. Lett.* **89**(11), 111113 (2006)
14. J.-F. Kischkat, External cavity quantum cascade lasers. Ph.D. thesis, Humboldt-Universität zu Berlin, Mathematisch-Naturwissenschaftliche Fakultät (2015)
15. A. Hugi, Single-mode and comb operation of broadband quantum cascade lasers. Ph.D. thesis, ETH Zürich (2013)
16. Y. Matsuoka, S. Mathonnière, S. Peters, W.T. Masselink, Broadband multilayer anti-reflection coating for mid-infrared range from 7 μm to 12 μm . *Appl. Opt.* **57**(7), 1645–1649 (2018). <https://doi.org/10.1364/AO.57.001645>
17. I. Gordon, L. Rothman, C. Hill, R. Kochanov, Y. Tan, P. Bernath, M. Birk, V. Boudon, A. Campargue, K. Chance, B. Drouin, J.-M. Flaud, R. Gamache, J. Hodges, D. Jacquemart, V. Perevalov, A. Perrin, K. Shine, M.-A. Smith, J. Tennyson, G. Toon, H. Tran, V. Tyuterev, A. Barbe, A. Császár, V. Devi, T. Furtenbacher, J. Harrison, J.-M. Hartmann, A. Jolly, T. Johnson, T. Karman, I. Kleiner, A. Kyuberis, J. Loos, O. Lyulin, S. Massie, S. Mikhailenko, N. Moazzen-Ahmadi, H. Müller, O. Naumenko, A. Nikitin, O. Polyansky, M. Rey, M. Rotger, S. Sharpe, K. Sung, E. Starikova, S. Tashkun, J. V. Auwera, G. Wagner, J. Wilzewski, P. Wcisło, S. Yu, E. Zak, The hitran2016 molecular spectroscopic database. *J. Quant. Spectrosc. Radiat. Transf.* **203**, 3–69 (2017). <https://doi.org/10.1016/j.jqsrt.2017.06.038>. <http://www.sciencedirect.com/science/article/pii/S0022407317301073> (hITRAN2016 Special Issue)
18. B.G. Lee, M.A. Belkin, R. Audet, J. MacArthur, L. Diehl, C. Pflügl, F. Capasso, D.C. Oakley, D. Chapman, A. Napoleone, D. Bour, S. Corzine, G. Höfler, J. Faist, Widely tunable single-mode quantum cascade laser source for mid-infrared spectroscopy. *Appl. Phys. Lett.* **91**(23), 231101 (2007). <https://doi.org/10.1063/1.2816909>